

Resonant features in the energy dependence of the rate of ketene isomerization

J. Daniel Gezelter and William H. Miller^{a)}

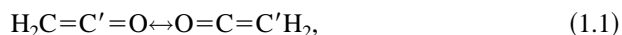
Department of Chemistry, University of California, and Chemical Sciences Division, Lawrence Berkeley Laboratory, Berkeley, California 94720

(Received 13 June 1995; accepted 8 August 1995)

Calculations of the microcanonical isomerization rates for vibrationally excited ketene are presented. The calculations utilize the quantum reactive scattering methodology of absorbing boundary conditions with a discrete variable representation to obtain the cumulative reaction probability for one form of ketene to isomerize via the oxirene intermediate, and were carried out with model 1-, 2-, and 3-degree-of-freedom potential energy surfaces constructed using *ab initio* data. Significant differences are seen in the energy dependent features of the microcanonical rate for the single mode and multi-mode potentials; e.g., the single mode potential exhibits tunneling resonances with widths of around 1 cm^{-1} , while the calculations involving more than one degree of freedom have additional resonant features that have widths around 10 cm^{-1} and also exhibit non-Breit–Wigner resonant line shapes. This suggests that many of the resonance features are best described as Feshbach (energy transfer, or dynamical) resonances that result because of a strongly bent region on the multi-mode potential energy surfaces. The calculated rates show reasonable qualitative agreement with the experimental results of Lovejoy and Moore [J. Chem. Phys. **98**, 7846 (1993)]. © 1995 American Institute of Physics.

I. INTRODUCTION

Lovejoy and Moore¹ recently reported some remarkable experimental results on the photodissociation and photoisomerization of ketene. Figure 1 shows a (much simplified) picture describing the situation; C and C' denote the isotopes carbon-12 and carbon-13, respectively. Very cold ketene (in a supersonic beam, $T_{\text{rot}} \sim 4\text{ K}$) is laser-excited to a well-defined energy E (energy resolution is $\sim 1\text{ cm}^{-1}$) and dissociation products (carbon monoxide and methylene) are observed. If the reactant molecule is $\text{H}_2\text{C}'\text{O}$, then the major product is CH_2 and $\text{C}'\text{O}$, but 10%–20% of the product has the isotopes of carbon switched, i.e., $\text{C}'\text{H}_2$ and CO , indicating that the isomerization,



has taken place prior to dissociation, presumably passing through the oxirene intermediate (cf. Fig. 1). (This isomerization or exchange process was also deduced from much earlier “hot atom” experiments by Rowland *et al.*)² From the branching ratio between normal and exchanged products, Lovejoy and Moore used a simple kinetic model to extract separately the unimolecular rate constants for direct dissociation (i.e., $\text{H}_2\text{C}=\text{C}'=\text{O} \rightarrow \text{H}_2\text{C}+\text{C}'=\text{O}$ without isomerization) and for isomerization, $k_d(E)$ and $k_{\text{iso}}(E)$, respectively. In a series of articles,³ Moore *et al.* have reported on many other interesting aspects of ketene photodissociation that are not the subject of the present article.

The energy dependence of $k_d(E)$ shows some interesting step structure due to quantization of the transition state, but is otherwise a very typical unimolecular $k(E)$ for which standard microcanonical transition state theory (i.e., RRKM⁴) is an excellent description. The isomerization rate

$k_{\text{iso}}(E)$, however, shows much more structure in its energy dependence, structure which Lovejoy and Moore attribute to metastable (resonance) states of oxirene. Resonance tunneling through a one-dimensional double barrier is a well-known phenomenon, but it has never (to our knowledge) been observed in a molecular process. (Under less well-defined experimental conditions, it would be easily averaged out.) Because of the novelty of this process, we therefore undertook a more detailed theoretical treatment, first to see if our theoretical methodology is capable of handling this complex reaction dynamics accurately for a polyatomic molecule of this size, and also to lend support (or not) to Lovejoy and Moore’s interpretation of their observed structure. This article describes these calculations and reports their results.

The microcanonical isomerization rate can be expressed as

$$k_{\text{iso}}(E) = \frac{N(E)}{2\pi\hbar\rho(E)}, \quad (1.2)$$

where $\rho(E)$ is the density of reactant (ketene) states per unit energy—which is a smooth, almost constant function of energy over the relevant region—and $N(E)$ is the cumulative reaction (here isomerization) probability (CRP), which contains all the aspects of the isomerization process and whose calculation is the central task. The development of theoretical methods for calculating CRPs has been a major focus of our research group in the last few years, so the present application is an excellent test of this methodology. Seideman and Miller’s⁵ expression for the CRP is

$$N(E) = 4\text{tr}[\hat{G}(E) * \hat{\epsilon}_p \hat{G}(E) \hat{\epsilon}_r], \quad (1.3)$$

where $\hat{G}(E)$ is the Greens function,

$$\hat{G}(E) = (E + i\hat{\epsilon} - \hat{H})^{-1}, \quad (1.4)$$

^{a)} Author to whom correspondence should be addressed.

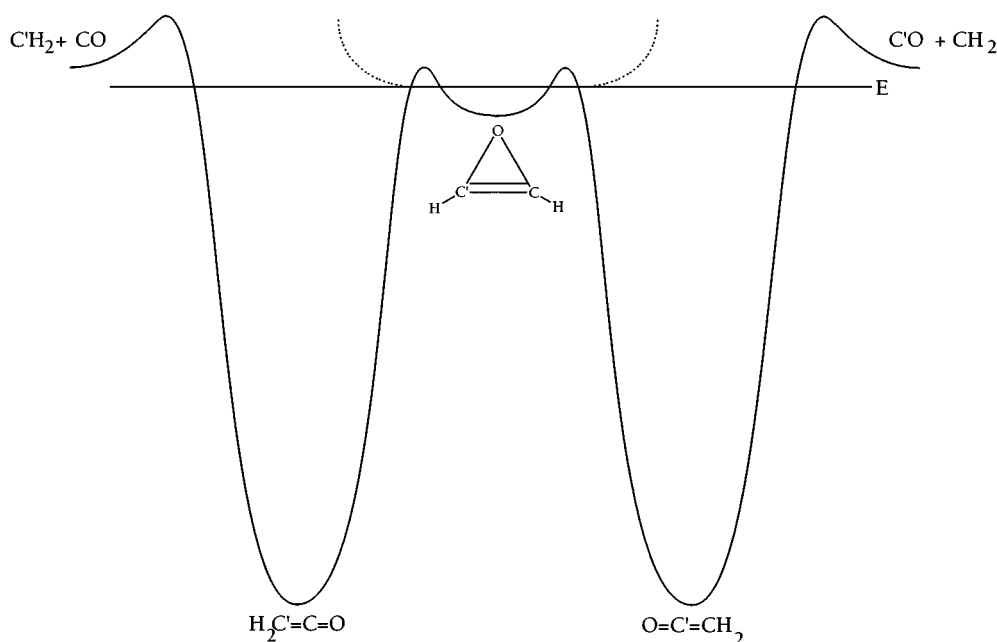


FIG. 1. A sketch of the relevant structures and energies involved in the photodissociation and photoisomerization of ketene.

\hat{H} being the total Hamiltonian for the ketene molecule and $\hat{\epsilon}$ an absorbing potential to enforce outgoing wave boundary conditions. $\hat{\epsilon}_r(\hat{\epsilon}_p)$ is the part of the absorbing potential in the reactant (product) region, e.g., the left (right) dotted curves in Fig. 1; $\hat{\epsilon} = \hat{\epsilon}_r + \hat{\epsilon}_p$. One may think of this quantum mechanical expression for the CRP as analogous to a classical trajectory calculation in which one starts trajectories in the left ketene well (cf. Fig. 1), with initial conditions sampled from a microcanonical distribution, and runs them to determine the fraction that reach the right hand ketene well, terminating them as soon as they exit the double barrier region into the product well. In this quantum calculation we are thus by-passing the problem of describing the dynamics of highly vibrationally excited ketene itself and only calculating the microcanonical reactive flux (which is the CRP).

Even with this limited treatment of the dynamics, however, it is not possible to carry out the calculation in its full dimensionality of $F = 3N - 6 = 9$ degrees of freedom (with total angular momentum $J=0$). We thus carry out a CRP calculation including f degrees of freedom, obtaining $N_f(E)$, and then fold in the other uncoupled degrees of freedom by microcanonical convolution,

$$N(E) = \sum_{n=0}^{\infty} N_f(E - \epsilon_u^{F-f}), \quad (1.5)$$

where $\{\epsilon_u^{F-f}\}$ are the energy levels—approximated as harmonic oscillators—for the $F-f$ uncoupled degrees of freedom, i.e., $n_j = n_{f+1}, \dots, n_F$, and

$$\epsilon_u^{F-f} = \sum_{j=f+1}^F \hbar \omega_j (n_j + \frac{1}{2}). \quad (1.6)$$

This is the idea of “dimensionality reduced” approximations,^{6,7} and for $f=1$ is the standard expression for one-dimensional tunneling corrections to microcanonical transition state theory.⁸

Section II first gives a more detailed description of the theoretical methodology and its implementation, and Sec. III describes the results of the calculation for $f=1, 2$, and 3 coupled degrees of freedom. Section IV concludes.

II. SUMMARY OF THEORETICAL AND COMPUTATIONAL SPECIFICS

A. The potential energy surface

The stability of the oxirene intermediate has been the subject of a great deal of controversy in the quantum chemistry community. Scott *et al.*⁹ have performed the most detailed calculation of the reaction path to date. At the CCSD(T)/6-311G(*df,p*) level of theory, they find a broad, corrugated well between the transition states that separate the two ketene structures, as shown in Fig. 2. The oxirene well, however, is only slightly stable and lies at an energy above the energy for formylmethylene. Frequencies for the oxirene structure have been obtained at the CCSD(T)-fc/TZ2P(*f,d*) level of theory by Vacek *et al.*¹⁰ This level of theory also shows oxirene to be a stable point on the potential energy surface.

Other levels of theory, including density functional theory, have given an imaginary frequency for the ring-opening mode of oxirene.¹¹ Most of these calculations also give a fairly broad central well with transition states between the formylmethylene structures and the associated ketene structures. The fact that the region between the two outer transition states is not a single minimum (as indicated in the

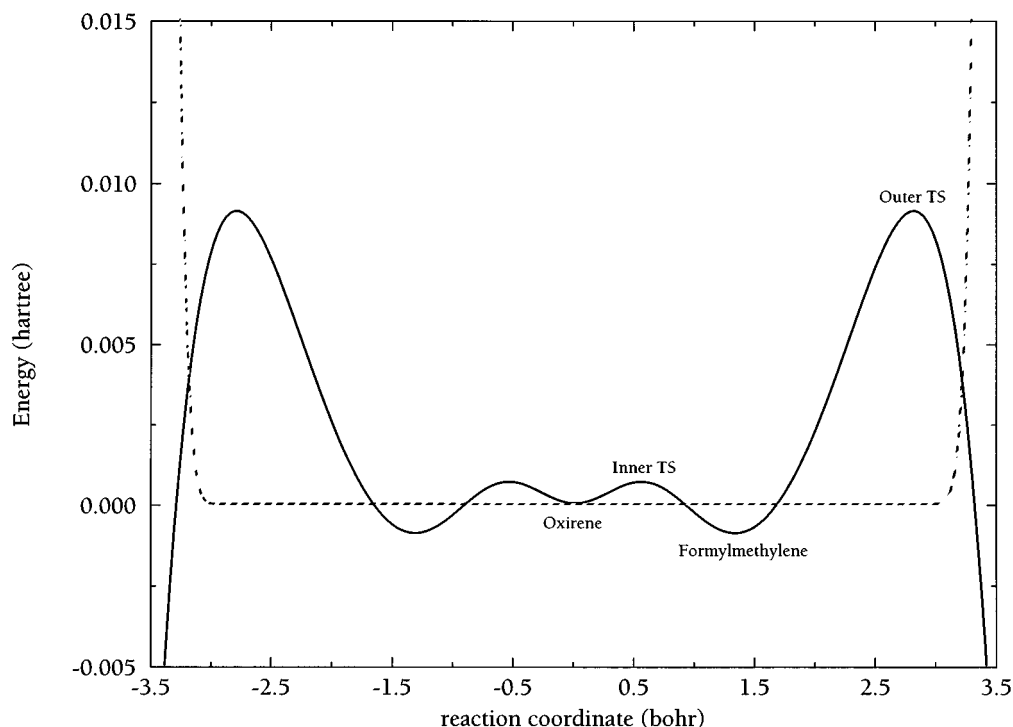
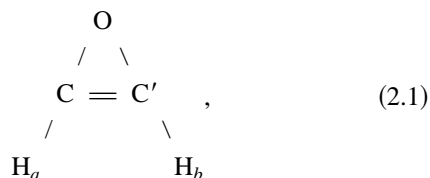


FIG. 2. A plot along the reaction coordinate showing the one-dimensional potential energy surface (solid line) and the absorbing potential (dotted line). The critical points are labeled with the names of the structures along the reaction coordinate that were calculated in Ref. 9.

simplified Fig. 1) does not change the discussion in the introduction about resonance tunneling, but it does suggest that the dynamics of the resonance intermediate may be quite complex.

We have used normal coordinates referenced to the oxirene geometry,



to construct a potential energy surface in the region of Fig. 2, incorporating all information available from *ab initio*⁹⁻¹¹ calculations as well as possible. From these calculations, we identify at least three degrees of freedom that play active roles in the isomerization process. (The carbon-carbon and one of the carbon-hydrogen bond lengths are largely unchanged throughout the isomerization.)

The first important normal mode coordinate—the one we identify as the reaction coordinate—involves mainly oxygen and hydrogen atom motion. Displacement along this normal mode describes most of the structural differences between oxirene and the intermediates that lie between oxirene and ketene.

We have identified the other two quantum degrees of freedom in terms of two of the *local* modes of oxirene. The second degree of freedom that we include in the quantum calculation is a linear combination of the a_2 CH asymmetric out-of-plane mode and the b_1 CH symmetric out-of-plane

mode. This corresponds to the out-of-plane motion of H_a relative to the CCO plane, a motion which has a frequency of approximately 514 cm^{-1} .

The third degree of freedom is a linear combination of the b_2 CH asymmetric rock and the a_1 CH symmetric rock. This combination corresponds to the in-plane swing of H_b towards the middle of the CC bond, and has a frequency of approximately 873 cm^{-1} .

We make some simplifying assumptions in calculating the frequencies of these local modes. The first assumption is that the asymmetric and symmetric normal modes are the normal modes for a system with two local modes which have identical frequencies. Next, we assume that the coupling between these local modes is positive. With these two assumptions, it is easily shown that the frequency of the symmetric normal mode is the same as the frequency of the constituent local modes. This is the lower of the two frequencies for each pair of normal modes listed above.

The form of the potential energy surface that we have used to perform this calculation is given by

$$V(s, \underline{Q}) = V_{1d}(s) + \sum_{j=2}^3 k_j \left(Q_j + \frac{f_j(s)}{k_j} \right)^2, \quad (2.2)$$

$$V_{1d}(s) = a_2 s^2 + a_4 s^4 + a_6 s^6 + c s^2 e^{-ds^2}, \quad (2.3)$$

and

$$f_j(s) = d_j s^4. \quad (2.4)$$

The parameters for the 1- d potential $V_{1d}(s)$ were obtained by fitting to the energies and structures in Ref. 9. A plot of

TABLE I. Energies and frequencies for the critical points along the reaction coordinate. Energies are relative to the oxirene structure.

		Oxirene	Inner TS	Formylmethylene	Outer TS
Energy (kJ/mol)	Best fit V_{1d}	0	1.8	-2.4	23.9
	Ref. 9 ^a	0	1.9	-2.0	23.9
ω (cm ⁻¹)	Best fit V_{1d}	134	141 <i>i</i>	152	277 <i>i</i>
	Refs. 9 ^b and 10	163 ^c	133 <i>i</i>	328	409 <i>i</i>

^aGeometries are optimized at the CCSD(T)/6-311G(df,p) level, and energies are calculated using a mean of CCSD(T)/cc-pVTZ(f) and CCSD(T)/cc-pVTZ(g) values.

^bCalculated at the CCSD(T)/6-31G(d) level.

^cCalculated at the CCSD(T)-fc/TZ2P(f,d) level.

this fit is given in Fig. 2. A comparison of the energies and frequencies of the calculated fit to the *ab initio* calculations is given in Table I.

Frequencies for the two coupled degrees of freedom were obtained from the frequencies for the asymmetric hydrogen rock (in plane) and asymmetric hydrogen wag (out of plane) modes calculated in Ref. 10. The coupling constants (d_j) for those two modes are obtained by using the geometries calculated in Ref. 9. A contour plot of the potential energy surface as a function of s and Q_2 is shown in Fig. 5, and all the parameters used in constructing the potential energy surface are given in Table II.

The absorbing potential, $\epsilon(s, Q_2, Q_3)$, that we use in our calculations is given by

$$\epsilon(s, Q_2, Q_3) = a \left(\frac{r - r_0}{r_{\max} - r_0} \right)^4 h(r - r_0), \quad (2.5)$$

where

$$r = \sqrt{c_s |s|^2 + c_2 |Q_2|^2 + c_3 |Q_3|^2}. \quad (2.6)$$

We place the beginning of the absorbing potential, r_0 , just after the final barriers to isomerization. The absorbing potential needs to rise fast enough to absorb the flux resulting from the rapid drop-off of the potential energy, so a polynomial of at least degree 3 is required for the form of ϵ . The end of the absorbing potential, r_{\max} is placed at the edge of the grid. This edge is located just far enough outside the barrier to isomerization to assure convergence.

TABLE II. Parameters of the best-fit potential energy surface.

Parameter	Value
a_2	-2.3597×10^{-3} (Hartree Bohr ⁻²)
a_4	1.0408×10^{-3} (Hartree Bohr ⁻⁴)
a_6	-7.5496×10^{-5} (Hartree Bohr ⁻⁶)
c	7.7569×10^{-3} (Hartree Bohr ⁻²)
d	1.9769 (Bohr ⁻²)
k_2	1.0074×10^{-2} (Hartree Bohr ⁻²)
d_2	-2.45182×10^{-4} (Hartree Bohr ⁻⁵)
k_3	2.9044×10^{-2} (Hartree Bohr ⁻²)
d_3	-8.54360×10^{-4} (Hartree Bohr ⁻⁵)

B. The basis set

We have used a discrete variable representation (DVR), i.e., a basis set of grid points, to represent the operators in Eq. (1.3), specifically the sinc-function DVR of Colbert and Miller.¹² The operators $\hat{H}, \hat{\epsilon}, \hat{G}$, etc., all become matrices in grid point space: $\underline{H}, \underline{\epsilon}, \underline{G}(E) = (E + i\underline{\epsilon} - \underline{H})^{-1}$.

We used a rectangular cartesian grid as the raw DVR grid for this problem. Points were removed from the grid if $V(s, Q)$ was greater than 2 times E , the energy for which we were calculating $N(E)$. Additionally, points that were outside a given r_{\max} , where r is defined in Eq. (2.6), were also removed from the grid. The number of points per deBroglie wavelength, N_B , was set to 3.7 for all calculations. The shortest possible deBroglie wavelength, which determines the grid spacing together with N_B , was obtained by taking the difference between E and the lowest point on the potential energy surface. Typical values for r_{\max} , and for the constants in Eqs. (2.5) and (2.6) are presented in Table III. For the 1-, 2-, and 3-degree-of-freedom calculations at the highest energy of interest, the number of remaining grid points in the truncated grids were 191, 4270, and 47836, respectively.

C. Evaluation of the trace

Manthe and Miller¹³ have shown that an efficient way to evaluate the trace in Eq. (1.3) is to introduce the reaction probability operator $\hat{P}(E)$, defined by

$$\hat{P}(E) = 4 \hat{\epsilon}_r^{1/2} \hat{G}(E) * \hat{\epsilon}_p \hat{G}(E) \hat{\epsilon}_r^{1/2}, \quad (2.7)$$

so that Eq. (1.3) for $N(E)$ becomes

$$N(E) = \text{tr}[\hat{P}(E)]. \quad (2.8)$$

TABLE III. Parameters of the absorbing potential.

Parameter	Value
r_0	2.7 (Bohr)
c_s	1
c_2	0.9
c_3	1
a	0.01 (Hartree Bohr ⁻⁴)
r_{\max} (1 <i>d</i>)	3.45 (Bohr)
(2 <i>d</i>)	4.3 (Bohr)
(3 <i>d</i>)	5.6 (Bohr)

[Since the absorbing potential matrices are diagonal, the square roots in Eq. (2.7) cause no problems.] The trace of \hat{P} in Eq. (2.8) is then evaluated using the Lanczos algorithm,^{14–16} i.e., one begins with some starting vector \underline{v}_1 , and a sequence of Krylov vectors is generated by

$$\underline{v}_{n+1} = \underline{P}(E) \cdot \hat{\underline{v}}_n + S.O., \quad (2.9)$$

where *S.O.* denotes Schmidt orthogonalization to all preceding vectors. The matrix elements of \underline{P} in this basis,

$$P_{n,n'} = \underline{v}_n \cdot \underline{P}(E) \cdot \underline{v}_{n'} \quad (2.10)$$

are obtained in the process of generating the vectors, and the trace carried out in this representation,

$$N(E) = \sum_n P_{n,n}. \quad (2.11)$$

This procedure is efficient because the rank of the matrix $\underline{P}(E)$ is low, typically orders of magnitude lower than the size of the DVR basis itself, and the number of Lanczos iterations required—i.e., the number of Krylov vectors which must be generated via Eq. (2.9)—is essentially the rank of \underline{P} .

We explicitly re-orthogonalize the Lanczos vectors to avoid compounding numerical errors and iterate until $N(E)$ is converged to 10^{-3} . For the highest energies reported this required 5–10 iterations, and for the lowest energies only about 3.

Every operation of the matrix \underline{P} onto a vector in Eq. (2.9) requires two operations of the Green's function matrix onto a vector [i.e., the various matrices in $\hat{P}(E) = 4\hat{\epsilon}_r^{1/2}\hat{G}(E)*\hat{\epsilon}_p\hat{G}(E)\hat{\epsilon}_r^{1/2}$ multiply sequentially from the right]. The operation of the Green's function matrix onto a vector effectively means that one must solve the set of linear equations,

$$\underline{A} \cdot \underline{x} = \underline{b}, \quad (2.12)$$

where the vector \underline{b} is given and $\underline{A} = (E + i\epsilon - H)$, and this is the primary computational task. Use of the Lanczos method above with the P -operator/matrix greatly reduces the number of Green's function operations that are required and is why it was such an important step forward.

There is, of course, an enormous literature on the solution of the linear algebra problem in Eq. (2.12). Our present matrix \underline{A} is complex symmetric, large, but very sparse. We have made most use of the generalized minimum residual (GMRES)¹⁷ and more recently the quasi-minimum residual (QMR) algorithms.¹⁸ These are both Krylov-based algorithms, and they allow one to use preconditioners, i.e., if \underline{A}_0 is an approximation to \underline{A} that itself is easily invertible, then one writes Eq. (2.12) as

$$\underline{A}' \cdot \underline{x} = \underline{b}', \quad (2.13)$$

where

$$\underline{A}' = \underline{A}_0^{-1} \cdot \underline{A} \quad (2.14)$$

$$\underline{b}' = \underline{A}_0^{-1} \cdot \underline{b}, \quad (2.15)$$

and then generates a Krylov basis using \underline{A}' . GMRES is the most efficient procedure on the basis of the number of such iterations, but it requires that one store (and explicitly or-

thogonalize) all the Krylov vectors. QMR is not as efficient as GMRES on the basis of number of iterations, but since it requires the storage of only a few Krylov vectors, its cost (i.e., computational time) per iteration is much less. QMR finds the inverse by a quasi-minimization of the residual at each iteration. It is based on the look-ahead Lanczos algorithm which is used to find approximate eigenvalues of large non-Hermitian matrices. We stop the QMR iterations when the residual for the Green's function has dropped below 10^{-4} .

We have found that a diagonal preconditioner gives the best performance with QMR, i.e.,

$$(\underline{A}_0)_{i,j} = (\underline{A})_{i,j} \delta_{ij} \quad (2.16)$$

in Eq. (2.14) above. Other preconditioners, notably the symmetric successive over relaxation (SSOR) preconditioner resulted in a smaller number of iterations, but the costs associated with finding the inverses of upper and lower Hessenberg matrices made it a less attractive preconditioner.¹⁹ For the particular matrices used in this calculation, SSOR was often more expensive than having no preconditioner at all.

III. RESULTS

A. Isomerization rate using one degree of freedom

The best-fit single mode potential energy surface (PES) is shown in Fig. 2, and the calculated cumulative reaction probability $N_{1d}(E)$ for this PES is shown in Fig. 3. $N_{1d}(E)$ was used to calculate the isomerization rate using the other eight vibrational modes at the outer transition states as uncoupled harmonic oscillators. The isomerization rate is shown as a solid line in Fig. 4. In all calculations, the experimentally measured^{3,20} density of states (4.5×10^4 states/cm⁻¹) for a reactant ketene molecule with 28 000 cm⁻¹ of vibrational energy was used.

With a single quantum degree of freedom, the rate shows resonant features with widths of $\sim 1-5$ cm⁻¹ that are spaced $\sim 70-80$ cm⁻¹ apart. From the $N(E)$ calculation in Fig. 3, this spacing corresponds to a progression of tunneling resonances within the one-dimensional oxirene well. Agreement with the experimental rate is surprisingly good, giving qualitative matches between the number of observed features and the absolute magnitudes of the rates.

B. Isomerization rate using two degrees of freedom

Using the two-mode potential energy surface displayed in Fig. 5 to calculate the microcanonical isomerization rate, two additional and striking aspects of the energy dependence of the rate are observed. Figure 6 shows the rate calculated using the reaction coordinate and the *out-of-plane* hydrogen mode as the two coupled degrees of freedom, and treating the other 7 modes as uncoupled harmonic oscillators. Resonant line shapes appear in the two-dimensional rates that resemble Fano line shapes instead of the pure Breit–Wigner peaks observable in the 1-*d* rates. This indicates that the background phase at those energies is nonzero, which we believe to be a signature of overlapping resonant contributions to the cumulative reaction probability.²¹

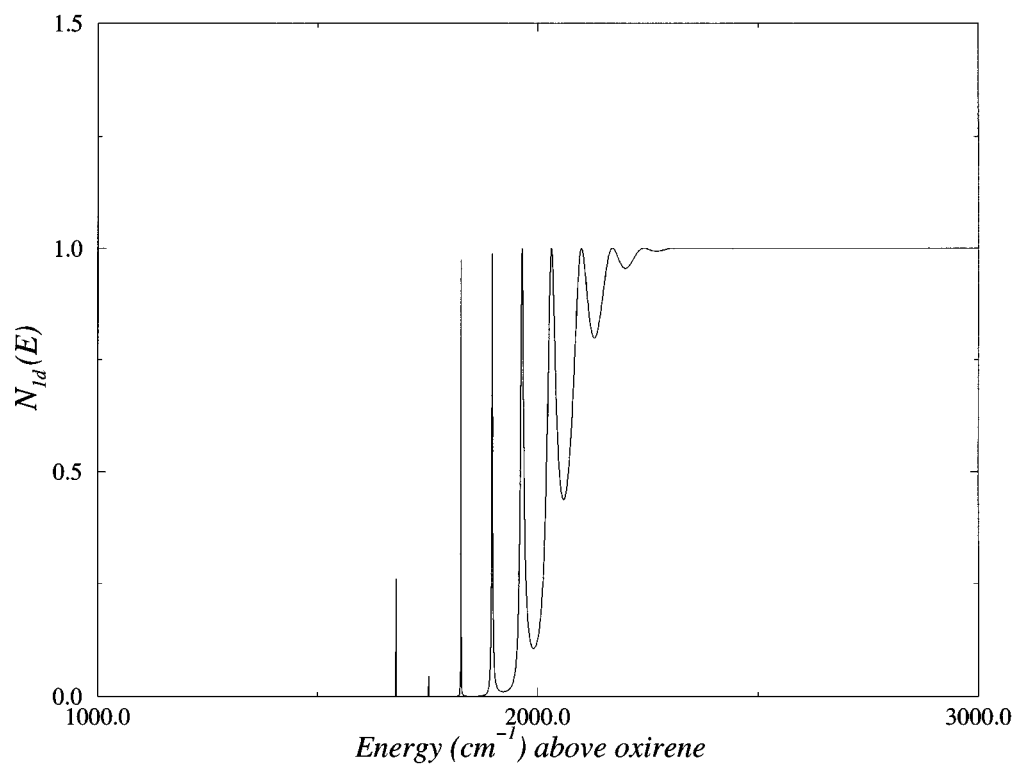


FIG. 3. The calculated cumulative reaction probability $N(E)$ for the potential shown in Fig. 2.

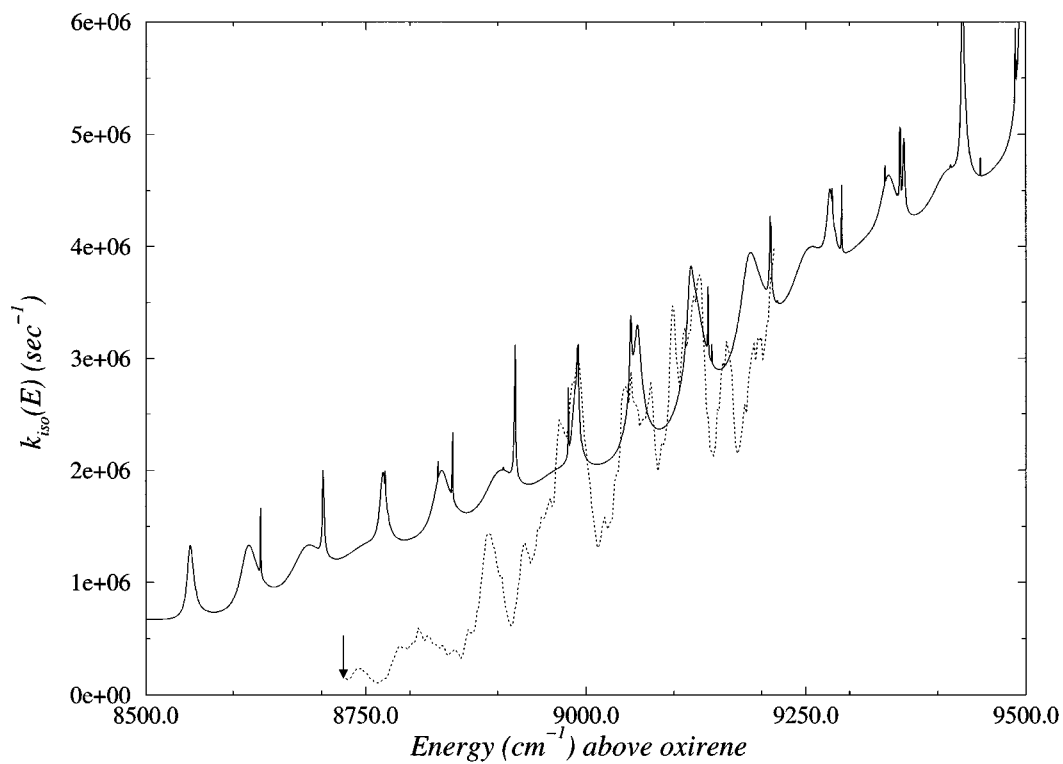


FIG. 4. The calculated isomerization rate for the one-dimensional surface shown in Fig. 2. The dotted line is the experimentally obtained reaction rate from Ref. 1.

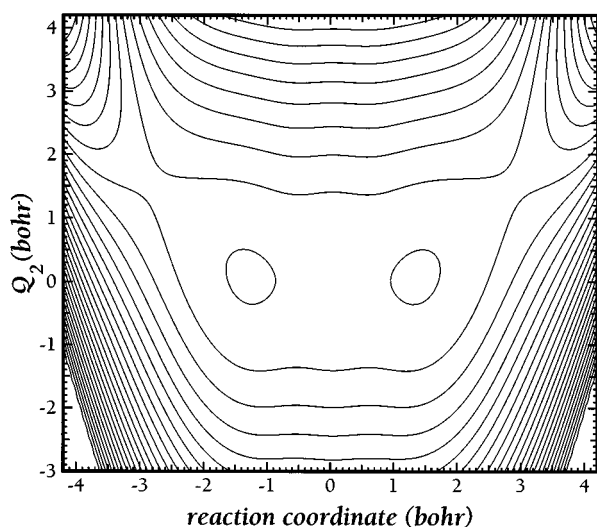


FIG. 5. A contour plot showing the two-dimensional potential energy surface (solid contours) and the absorbing potential (dashed contours). The two degrees of freedom represented in this plot are the reaction coordinate, s , and the hydrogen out-of-plane local mode, Q_2 .

The other striking feature is that there are resonant features that are wider ($\sim 10 \text{ cm}^{-1}$) than those observed in the one-degree of freedom rate. We believe that these features correspond to Feshbach, energy-transfer, or dynamical resonances that occur at energies above the barrier to isomerization. These dynamical resonances appear because the multi-mode potential energy surface has a strongly bent region

between the two outer transition states (cf. Fig. 5), which acts as a dynamical bottleneck even at total energies above the outer transition state energies.

Figure 7 shows the two-dimensional rate calculated using the reaction coordinate and the *in-plane* hydrogen mode as the two coupled degrees of freedom, and treating the other seven modes as uncoupled harmonic oscillators. As in the other two-dimensional calculation, resonance widths are wider (10 cm^{-1}) than in the one-dimensional calculation and the spacings between the wide resonant features are on the order of $70\text{--}80 \text{ cm}^{-1}$. Most of the peaks are pure Breit-Wigner-type peaks, which indicates that there are very few overlapping resonances when the *in-plane* mode is used as the second coupled degree of freedom. This is due in large part to the higher vibrational frequency of the *in-plane* mode relative to the out-of-plane mode's vibrational frequency.

C. Isomerization rate using three degrees of freedom

We have also calculated $k_{\text{iso}}(E)$ for three coupled degrees of freedom (i.e., the reaction coordinate, the *in-plane*, and the out-of-plane hydrogen local modes are coupled according to the parameters for the potential energy surface given in Table II). The isomerization rate for the three-dimensional calculation is shown in Fig. 8. It exhibits broad (10 cm^{-1}) features similar to the ones that were observed in the two-dimensional rates, as well as a few overlapping resonances similar in character to the ones present in Fig. 7.

We attribute the narrow (1 cm^{-1}) features that are similar to the ones observed in the one-dimensional calculations

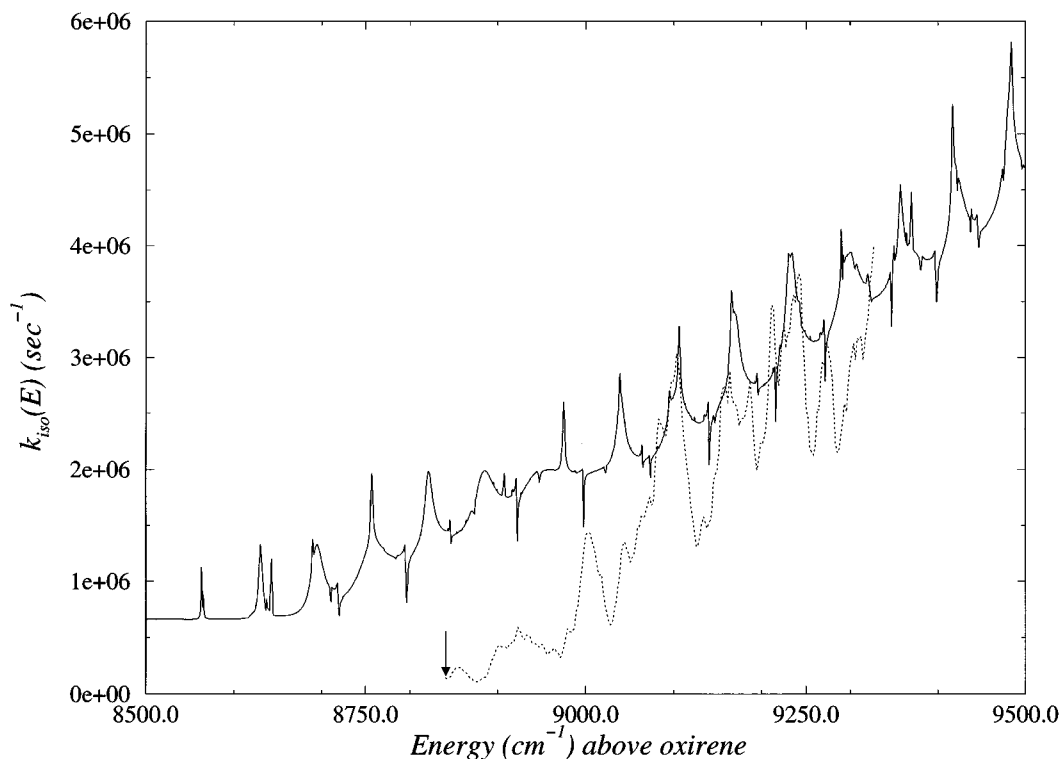


FIG. 6. The calculated isomerization rate for the two-dimensional surface shown in Fig. 5. The dotted line is the experimentally obtained reaction rate from Ref. 1.

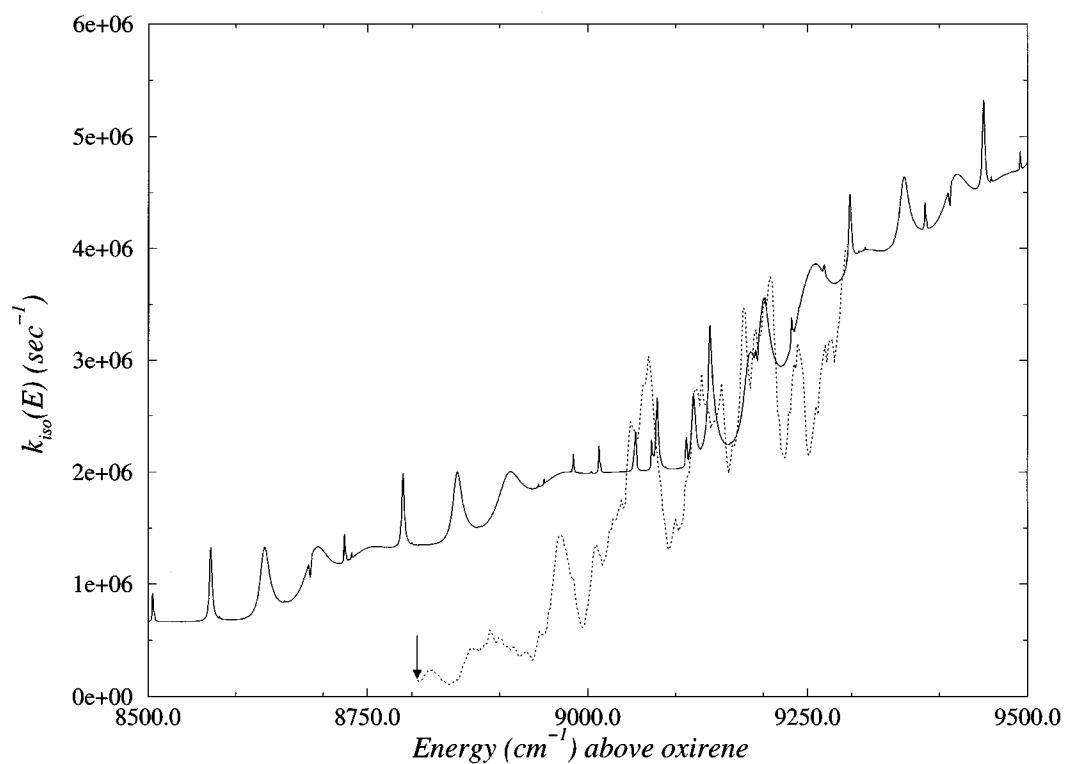


FIG. 7. The calculated isomerization rate for a two-dimensional surface using the reaction coordinate, s , and the hydrogen in-plane local mode, Q_3 . The dotted line is the experimentally obtained reaction rate from Ref. 1.

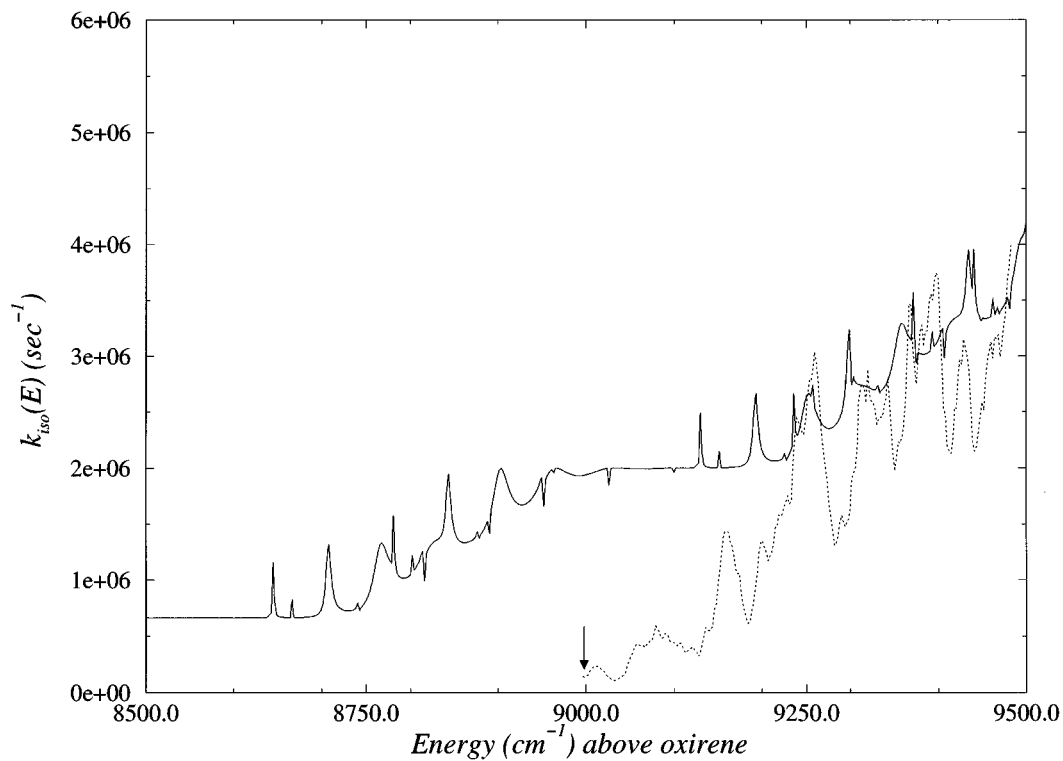


FIG. 8. The calculated isomerization rate for a three-dimensional surface using the reaction coordinate, s , and both the hydrogen out-of-plane local mode, Q_2 , and the in-plane local mode, Q_3 . The dotted line is the experimentally obtained reaction rate from Ref. 1.

to tunneling resonances. These features are observed at energies below the barriers to isomerization (at $\sim 8100\text{ cm}^{-1}$ in Figs. 4, and 6–8). The narrow features can also be observed at higher energies because of repetitions due to the uncoupled harmonic modes. At energies well above the barrier to isomerization, we again see the broad features that we attribute to Feshbach resonances that were observed in the two-dimensional isomerization rates.

IV. DISCUSSION

In Figs. 4, 6, 7, and 8, the calculated rates (solid lines) are plotted along with the experimental rates (dashed lines). However, since the present experiments determine the isomerization rate indirectly, i.e., from the exchange yield of the labeled carbon atom in the dissociation of ketene into CO and CH₂, they cannot measure the isomerization rate below this dissociation threshold. The barrier to dissociation lies slightly above the barrier for the isomerization, and the relative energies of these two barriers are only known to within a few hundred cm^{-1} , so we have adjusted the zero of energy for the experimental rate to illustrate the kind of agreement that our calculations can give with the experimental rates. The energy that we have assumed as the barrier to dissociation is marked with an arrow along the energy axis in each of these figures. It would be very useful to have experimental results for the isomerization rate below the dissociation threshold, for this would confirm or deny the existence of true tunneling resonances that lie below the barrier to isomerization.

Additionally, by placing absorbing potentials immediately outside the outer transition state between the oxirene well and ketene, we have eliminated any interaction between the dynamics within the ketene wells and the oxirene region. It is possible that these interactions could alter the theoretically calculated rates to some degree. However, these calculations are performed at energies where there is a near-continuum of states in the ketene well, and we expect that the mixing of the ketene states that occurs prior to isomerization will average out the effects of the interaction between the two regions.

The model potential surfaces presented in Sec. II are obviously not close enough to the true surface to give us quantitative agreement with the experimental rate. Also, although we have included up to three of the most strongly coupled degrees of freedom relevant to the isomerization process, incorporating other degrees of freedom fully dynamically (and not just via the reduced dimensionality approximation) will undoubtedly change the results somewhat. Nevertheless, we do see qualitative similarities between the present calculated rates and the experimental results. The average width and spacing of the features in the isomerization rate are represented well in our calculations, leading us to believe that we have included most of the important large-scale features of the potential energy surface in our current model.

Perhaps the most definite conclusion that we can draw is that the resonances structure in the isomerization rate is not

from purely tunneling resonances. Tunneling is the only decay mechanism of a metastable oxirene state in one dimension, but the widths of the resonant features in the one-dimensional calculation are much narrower than the structure seen experimentally. Multidimensional models allow also for Feshbach, or energy-transfer (dynamical) resonances: here the metastable state has enough total energy to dissociate (without tunneling) but not enough energy in the reaction coordinate; the decay rate (resonance width) is determined in this case by the rate of energy transfer from a “bath” mode into the reaction coordinate. Both tunneling and multimode coupling are of course included in the multidimensional calculations, and the significantly broader resonance features indicate that Feshbach-type resonances make a very significant contribution to the ketene isomerization. This is easily understood from the strong curvature seen in the multidimensional potential energy surfaces.

ACKNOWLEDGMENTS

The authors would like to thank Ned Lovejoy, George Vacek, and Professors C. B. Moore, H. F. Schaefer III, and N. C. Handy for many helpful discussions. This work was supported by the Director, Office of Energy Research, Office of Basic Energy Sciences, Chemical Sciences Division of the U.S. Department of Energy under Contract No. DE-AC03-76SD00098.

- ¹E. R. Lovejoy and C. B. Moore, *J. Chem. Phys.* **98**, 7846 (1993).
- ²C. C. Chou and F. S. Rowland, *J. Chem. Phys.* **50**, 5133 (1969).
- ³S. K. Kim, E. R. Lovejoy, and C. B. Moore, *J. Chem. Phys.* **102**, 3202 (1995); I. Garcia-Moreno, E. R. Lovejoy, and C. B. Moore, *ibid.* **100**, 8890 (1994); E. R. Lovejoy, S. K. Kim, and C. B. Moore, *Science* **256**, 1541 (1992).
- ⁴O. K. Rice and H. C. Ramsperger, *J. Am. Chem. Soc.* **50**, 617 (1928); L. S. Kassel, *J. Phys. Chem.* **32**, 1065 (1928); R. A. Marcus and O. K. Rice, *J. Phys. Colloid Chem.* **55**, 894 (1951); R. A. Marcus, *J. Chem. Phys.* **20**, 359 (1952).
- ⁵T. Seideman and W. H. Miller, *J. Chem. Phys.* **97**, 2499 (1992).
- ⁶J. M. Bowman, *J. Phys. Chem.* **95**, 4960 (1991).
- ⁷J. V. Micheal, J. R. Fisher, J. M. Bowman, and Q. Y. Sun, *Science* **249**, 269 (1990).
- ⁸W. H. Miller, *J. Am. Chem. Soc.* **101**, 6810 (1979).
- ⁹A. P. Scott, R. H. Nobes, H. F. Schaefer III, and L. Radom, *J. Am. Chem. Soc.* (in press).
- ¹⁰G. Vacek, J. M. Galbraith, Y. Yamaguchi, and H. F. Schaefer III, *J. Phys. Chem.* **98**, 8660 (1994).
- ¹¹N. C. Handy (private communication).
- ¹²D. T. Colbert and W. H. Miller, *J. Chem. Phys.* **97**, 1982 (1992).
- ¹³U. Manthe, T. Seideman, and W. H. Miller, *J. Chem. Phys.* **101**, 2652 (1994).
- ¹⁴C. Lanczos, *J. Res. Natl. Bur. Stand.* **45**, 255 (1950).
- ¹⁵J. H. Wilkinson and C. Reinsch, in *Handbook for Automatic Computation* (Springer, New York, 1971), Vol. II.
- ¹⁶J. K. Cullum and R. A. Willoughby, *Lanczos Algorithms for Large Symmetric Eigenvalue Computations* (Birkhauser, Boston, 1985).
- ¹⁷Y. Saad and M. H. Schultz, *SIAM J. Sci. Stat. Comput.* **7**, 856 (1986).
- ¹⁸R. W. Freund, *SIAM J. Sci. Stat. Comput.* **13**, 425 (1992).
- ¹⁹S. Eisenstat, *SIAM J. Sci. Stat. Comput.* **7**, 856 (1986); H. Karlsson and W. H. Miller, *J. Chem. Phys.* (submitted).
- ²⁰E. R. Lovejoy, S. K. Kim, R. A. Alvarez, and C. B. Moore, *J. Chem. Phys.* **98**, 7846 (1993).
- ²¹J. R. Taylor, *Scattering Theory* (Wiley, New York, 1972).